Technical Article

Study on the Effects of Stator Segmentation on the Characteristics of an Electrical Vehicle Traction Drive

Abstract — **To utilize manufacturing advantages, e.g. using prewound single teeth, stator cores for electrical machines can be segmented. The connection between the single teeth has to be mechanically sturdy, while the influence on the electromagnetic performance must be minimal. The influences of the segmentation of the stator and of the fit assembly with the stator housing are examined in this article with regard to the electromagnetic behavior. The influence of manufacturing tolerances is considered as well. First, the influence of mechanical stress on the magnetization behavior of ferromagnetic solids based on the magnetostriction and the magneto-mechanical (Villari effect) is presented. Furthermore, measurements of the Villari effect are presented, which are used to model this effect in the electromagnetic simulation. Subsequently, the fit assembly of the stator segments in the stator carrier is calculated by means of a 2D finite element simulation. The mechanical stress behavior and the deformation of the stator segments are determined and analyzed for different tolerance levels. Using the results of the mechanical simulation, the geometry for the electromagnetic simulation is derived. The machine is simulated in an electromagnetic way, taking into account the stress dependent material behavior. The influence of mechanical stress and the deformation of the segments is studied. The flux density in the stator yoke and the air gap of the machine, as well as the torque and the iron losses are evaluated. The results are analyzed exemplarily for the corner point of the machine with maximum torque. The different tolerance positions of the machine are taken into account.**

I. Introduction

The increasing electrification of the automotive powertrain will be significant in the next few years. It will lead to a growth in the production of electrical machines [1]. In order to reduce costs in the area of large-scale production, automated production of the electrical machines is necessary [2]. A challenge in the automated production of electrical machines is the winding. For electrical machines with concentrated windings, it is possible to build up the stator segmented, so that the teeth can be wound and insulated before assembly [3]. Concentrated windings offer the advantages of a small winding head length and a high copper fill factor [2, 4, 5]. When punching out the segments from the electrical steel, this design also produces less waste [3, 6, 7].

The wound and insulated segments can be assembled in a stator housing using a fit assembly which fixes the segments against each other and is used as a torque support. The stator segments are compressed during this process. This results in a mechanical stress in the segments, which counteracts the deformation. The magnetic behavior of soft magnetic materials shows a dependence on the mechanical load [8, 9, 10]. The Villari effect describes this behavior. So it can be assumed that the magnetization behavior of electrical machines is influenced by the mechanical stress load of the fit assembly. Due to the segmentation, additional air gaps are placed into the magnetic circuit. As a result of the fit assembly, displacements occur which can cause a change in the air gap width of the machine.

The manufacturing process of electrical machines leads to deviations and uncertainties in the design. Like all manufacturing processes, only a finite manufacturing accuracy is achievable, so that each manufactured component has a deviation from its ideal properties. In multi-stage manufacturing processes, these deviations of the individual components accumulate, so that the influence of manufacturing deviations in segmented electrical machines must be considered separately.

The influences of the stator's segmentation and of the fit assembly are examined in this article with regard to the electromagnetic behavior. The influence of manufacturing tolerances is considered. As an example machine, a permanent magnet synchronous machine with concentrated windings is selected. First, the mechanical fit assembly of the stator segments in the stator housing is calculated. The mechanical stress behavior and the deformation of the stator segments are investigated and analyzed for different tolerance levels. Using these results, the geometry for electromagnetic calculations is then derived and the machine calculated, taking into account the stress-dependent material behavior. Electromagnetic simulations are used to investigate the influence of the mechanical stresses and the deformation of the segments on the magnetic flux density in the stator yoke and in the air gap of the machine, as well as on the torque and the iron losses. The considered operating point corresponds to the corner point of the machine with maximum torque. The different tolerance levels of the machine are taken into account.

II. Magnetic Material Behavior Influenced by Mechanical Load

A. Magneto-Mechanical Effect

When a material is exposed to a magnetic field, deformation occurs in the direction of magnetization. This effect was discovered by Joule in 1842 and is called magnetostriction [11]. The existence of the magnetostriction implies, conversely, that mechanical stress influence the magnetization behavior. If the mechanical stress acts only in one spatial direction, this effect also leads to an anisotropic material behavior called the Villari effect [11]. For positive magnetostrictive materials, tensile stress of the sample in the direction of the magnetic field results in better magnetization behavior. The relative permeability μ_r increases because the formation of a uniform domain is favored by the tensile stress. The magnetization curve is steeper under mechanical tension. For compressive stress, the material has a poorer magnetization behavior. The magnetic permeability is lower and the magnetization curve flattens off. If the hysteresis curves are considered instead of the magnetization curve, a compression of the hysteresis curve for mechanical tensile stress and an expansion of the hysteresis curves for mechanical compressive stress can be observed. For a material with negative magnetostrictive behavior, this effect reverses and the magnetization increases at mechanical compressive stress.

B. Measurement of Magneto-Mechanical Effect

To measure the load-dependent material behavior, a standardized single-sheet-tester measuring instrument with attached hydraulic cylinder as shwon in Figure 1 is used [12]. Through the cylinder, a homogeneous mechanical stress of $\pm 100\,\mathrm{MPa}$ can be introduced into the sample. The force vector is collinearly

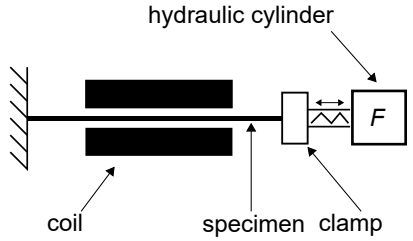

Fig. 1. Single-Sheet-Tester with Hydraulic Cylinder.

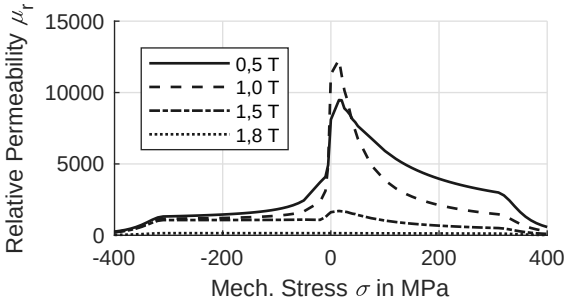

(a) Extrapolation of measured values for relative permeabilty.

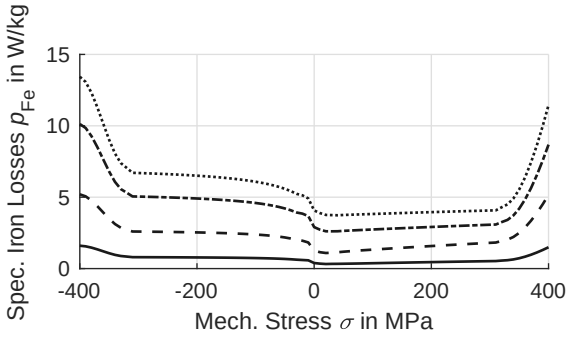

(b) Extrapolation of measured values for specific iron losses.

Fig. 2. Extrapolation of measured values for (a) relative permeabilty μ_r and (b) specific iron losses (at 50 Hz) dependent on mechanical stress σ for various magnetic flux densities B.

imposed on the magnetic field vector, so that a scalar relationship between the magnetic quantities and the mechanical stress can be determined. The sample tends to bent under a compressive mechanical load. A homogeneous mechanical force distribution can only be guaranteed for a compressive stress under a certain threshold value that mostly depends on the thickness of the specimen. In this case the maximum adjustable mechanical compressive stress in this series of tests is -20 MPa.

The material used for this series of measurements is electrical steel grade M400-50A. The measurements are carried out along the rolling direction. Further work in [13] explains the influence of the rolling direction on the magnetic properties.

C. Measurement Results

Figure 2 shows the characteristic stress-dependent magnetic material properties, such as relative permeability curves and specific iron losses. A significant dependence of the magnetic properties on the mechanical stress can be observed. In particular, mechanical compressive stress leads to a decrease in the relative permeability and an increase in specific iron losses. In the tensile stress part, there may initially be a decrease in specific losses before the losses increase in this area as well. The increase is less pronounced than in the compressive stress range.

As explained in section B, sample bending limits the measurable compressive stresses to -20 MPa. In the electrical machine, mechanical stresses outside the measuring range are expected due to the structure of the fit assembly. For these areas, the magnetic properties are expanded. Based on measurements from [14] for higher mechanical compressive and tensile stresses and [8] for mechanical stresses in the plastic range.

For tensile loads over 100 MPa, the relative permeability μ_r continues to decrease, but more slowly. With this behavior, the material can be described up to the yield strength $R_{p0.2}$. In the area of plastic deformation, the permeability decreases almost quadratically. After reaching $R_{p0.2}$, the relative permeability drops within a few 10 MPa by a factor of two to three [8]. For the losses, a similar, reverse behavior as for the relative permeability can be seen. The losses increase steadily in the elastic range and increase by a factor of two to three in the area of plastic deformation.

One way to set high compressive loads in a sample is to measure a sample as a lamination stack [14]. As the compressive stress increases, a saturation effect in relative permeability occurs. Relative permeability does not decrease significantly from -150 MPa. The permeability in this range is independent on the magnetic flux density B. The losses and the relative permeability have a slight saturation effect for increasing compressive load, too. However, they are still dependent on the magnetic flux density B even under high compressive load. Findings on material behavior can be confirmed with further measurements from [15], [9] and [10]. The influence of axial mechanical stress on the magnetic properties of non-oriented electrical steel is elaborated in [16].

III. Mechanical Model

To determine the influences of the segmented stator design, a mechanical simulation of the fit assembly connection is performed. The mechanical stress in the stator segments is of special interest, as well as the resulting radial displacement of the stator tooth tip.

A. Modelling of the Fit Assembly

Two approaches are possible for this kind of two dimensional finite element simulation: The plain stress or the plain strain approach [17]. The real behavior is in between both simulation approaches and either one can be used for the present geometries and properties. The plain stress approach is chosen because of its tendency to depict a higher stress.

The mechanical simulation model consists of two stator segment parts and the stator housing. They represent the smallest possible symmetry and are shown in Figure 3.

The middle of each stator segment is used as the symmetry boundary condition and a frictionless contact is applied. For the other contacts between stator segments and also between stator segment and stator carrier a friction coefficient of 0.2 is supposed. This matches the coefficient for static friction of steel on steel [18]. The simulation assumes a symmetrical contact behavior. To calculate the contacts the Augmented Lagrange Algorithm is used [17, 19]. The mesh of the model considers multiple influences. Because of its complex geometry it is not trivial to calculate the deformation and resulting stress at the tip of the stator segment key. The highest mechanical stress is expected at the tip of the key and the wings of the slot. Small air gaps between the key and the slot geometry are also critical for the calculations of the model. To avoid singularities and resulting convergency problems, the small air gaps cannot be meshed too fine [19]. The same problem applies to the tip of the stator segment key and slot. These points exhibit comparatively high

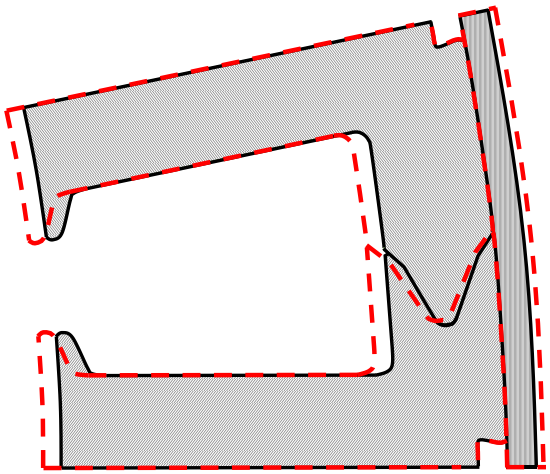

Fig. 3. Simulated symmetry and expected displacement (dashed).

stress and plastic strain and can cause convergency problems as well [20]. The mesh for the mechanical model is balanced to achieve the most accurate results while being robust against singularity effects at the contact surfaces.

The mechanical simulation is based on Hooke's law for the calculation of the elastic stress and strain. For the case of ideal isotropy, assumed here, the Hooke matrix can be characterized by the Young's modulus E and the Poisson's ratio ν [21]. Hooke's law only applies up to the proportional limit from which on the mechanical stress does not correlate linearly with the mechanical strain. This then is called a plastic deformation [21] for which a different calculation model is needed. The material model of Ludwik is usually employed for mechanical simulations with small plastic deformations [22]. Such plastic deformations are only expected in the key slot area of the stator segments. For the stator carrier a pure elastic material model is applied. An electrical steel of the quality M400-50A with yield strength of 340 MPa is used for the stator segments. The stator carrier consists of an unalloyed steel with the quality DC04. To quantify the mechanical stress the von Mises equivalent stress is used. It is derived from the shape modifying energy of solid materials [23]. The equivalent stress model is applicable for ductile solids and also represents the yielding region.

An alternative method to describe a stress condition is Mohr's circle. It projects a stress condition on a circle within a coordinate system of the shear stress τ and the normal stress σ. A comprehensive derivation can be found in [18]. According to Mohr every stress condition can be transfered into a state without shear stress. Therefore a coordinate system rotation is applied to the stress condition described by the normal stresses σ_x and σ_y as well as the tangential tension τ_{xy}. In this state the normal stresses σ'_x and σ'_y are termed principal stresses. No shear stress exists in the direction of the principal stresses [18]. This transformation is necessary to map the mechanical stresses onto the electromagnetic simulation since stress-dependent material parameters are only available for uniaxial stress conditions. To evaluate the deformations the von Mises displacement is used.

B. Influences of Manufacturing Tolerances

The described mechanical simulation of the fit assembly is now used to evaluate the influences of the manufacturing tolerances of stator carrier and stator segments on the mechanical stress and displacement. The components exhibit four tolerances relevant for the fit assembly. The inner diameter of the stator carrier

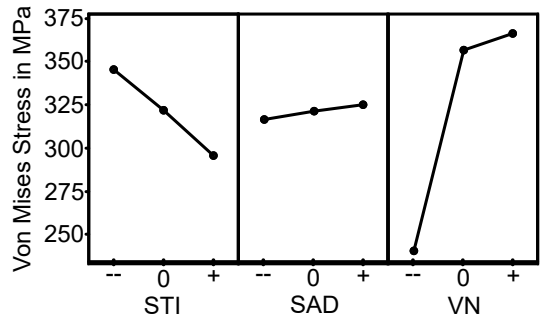

(a) Principal effect diagram of the maximal von Mises stress.

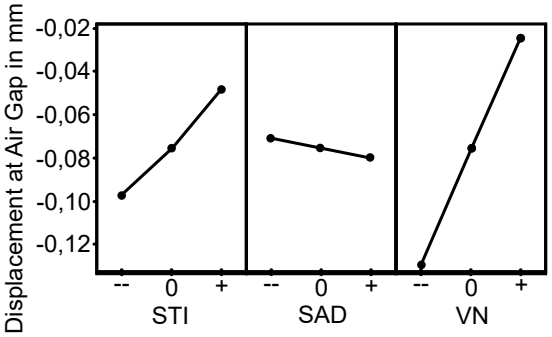

(b) Principal effect diagram of the maximal tooth tip displacement.

Fig. 4. Results of the sensitivity analysis in the form of principal effect diagrams.

has a bidirectional tolerance range and therefore can show positive as well as negative deviations. The stator segment exhibits unidirectional profile tolerances on all contact surfaces. These only allow positive deviations. Because of the interaction of key and slot the tolerances of this connection are not varied independently. The tolerances are varied in combinations which represent the wear of the stamping tool. So for example both tolerances of the stator segment are either nominal or maximal.

To study the influence of the manufacturing tolerances on the target figures a sensitivity analysis is conducted. To identify interdependencies as well as nonlinear influences a three stage full factorial design of experiments is applied. The defined target figures are the maximal von Mises stress in the stator segment and the maximal displacement of the stator segment tooth tip. The nominal model represents the manufacturing and assembly of a dimensionally accurate stator. Originating from this reference point 26 more combinations are simulated.

C. Results and Discussion

The simulated results for each parameter variation are visualized in the principal effect diagram in Figure 4.

The key slot tolerance (VN) exhibits the highest influence on the occuring von Mises stress and the tooth tip displacement. The stator outer diameter tolerance (SAD), which is significantly smaller than the stator carrier inner diameter tolerance (STI), shows little influence on the target figures. The evaluation of the isolated principal effects shows a possible variation in stress of over 100 MPa. The tooth tip displacement can vary around 0.1 mm. This can be translated into an air gap variation of up to 10 % for a 1 mm air gap.

The influence of the key slot geometry on the mechanical stress shows a nonlinear behavior. This results from the mechanical design of the stator segment connection. For the nominal geometry occurs only a slight deformation of the slot wings with the aforementioned air gap between key tip and slot ground. For higher pressings the air gap is eliminated and plastification oc-

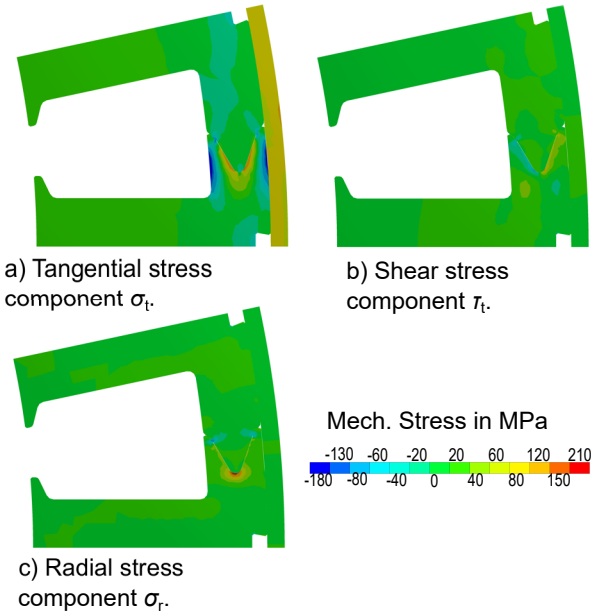

Fig. 5. Tangential-, shear- and radial component of the mechanical stress for the nominal model.

curs in the key tip region. The hereby occurring stresses are significantly higher compared to the nominal state without contact in the key tip area. After the first plastification the stress level only rises moderately even for higher pressings. The influences of the tolerances of stator carrier inner diameter and stator segment outer diameter behave linearly. Equally linearly behave the influences of all three tolerance ranges on the tooth tip displacement. A significant interdependency is only apparent between the parameters stator carrier inner diameter and key slot for the target figure maximal stress.

The von Mises equivalent stress does not differentiate between tensile and compressive mechanical stress. However the magnetic behavior of electrical steel differs significantly depending on tensile or compressive stress. To analyze the stress states in the machine a cylindrical coordinate system is used. This enables the separation of the occurring mechanical stress in its tangential, radial and shear component. The three stress components for the nominal state are pictured in Figure 5. A positive sign stands for tensile stress and a negative sign for compressive stress.

The tangential stress component represents the largest portion of the stress state. The stator carrier exhibits a sole tensile load caused by the expansion. As expected the stator yoke exhibits mainly compressive stress, except for the key slot area. The radial and shear stress components are almost zero outside the key slot area. At the outsides of the slot wings the extension leads to compressive stress. Tensile stress is visible at the inner side of the slot through the tangential stress component. At the outer part of the key slot area occurs compressive stress in radial direction. Radial stress is visible at the inside of the slot wing. This radial stress arises because of the spreading of the wings. Since the key slot geometry is not tangentially aligned, shear stress is apparent as well. Only tangential compressive stress would be visible in an unsegmented stator, opposed to the tensile stress visible in the stator carrier. Yet the segmented design and pronounced key slot geometry lead to a more complex stress state.

Relevant parameter combinations are chosen to resemble limiting cases and are simulated in addition to the sensitivity analysis. The parameters are defined in a way that they represent the minimal, middle and maximal pressing. The von Mises stress of the simulated limiting cases is pictured in Figure 6.

As expected, the results show significant differences between the three cases. The radial displacement of the tooth tip can vary between -0.148 mm and 0.03 mm whereby the negative displacement represents an air gap width reduction. This means that an air gap width variation of over 15 % is possible. This can effect the torque and power output of the machine significantly [24, 25, 26]. The parameter combination for the minimal pressing shows stress levels of up to 200 MPa in the key slot area. The stress is concentrated on the key slot area and has almost no effect on the rest of the stator yoke. The middle pressing case shows larger areas of the stator yoke under stress and an average stress level of 70 MPa. The maximal pressing exhibits mechanical stress up to 390 MPa in the key slot area which leads to plastification. In this case the mechanical stress level in the yoke is betweeen 90 MPa and 180 MPa. The results of the mechanical simulation show a significant influence of the parameters and their tolerance ranges on the resulting mechanical stress and displacement. For this reason the transfer of the stress and displacement results into the electromagnetic simulation is necessary to asses the influence of the Villari effect and the air gap width variation on different electromagnetic target figures.

IV. Electromagnetic Model

For the electromagnetic simulation of the considered machine, the partial model of a pole pair is set up. By means of static mechanical simulation – using the deformation solution of the mechanical simulation – the geometry of the machine with deformed stator is built up. Subsequently, the boundary conditions, the mesh and the suggestions of the electromagnetic simulation are described. The torque characteristics of the machine are simulated and the iron losses are considered.

Equivalent to the procedure described in the Section III, a mechanical simulation of a pole pair is carried out with which the geometry of the stator segments can be imaged after installation in the stator carrier. A pole pair consists of three stator segments. For the three stator segments, the deformation solution for each node of the model is calculated in the mechanical simulation. The deformed geometry is then used to construct the pole pair model of the machine with windings, rotor and magnets. The stator carrier is not considered for the electromagnetic

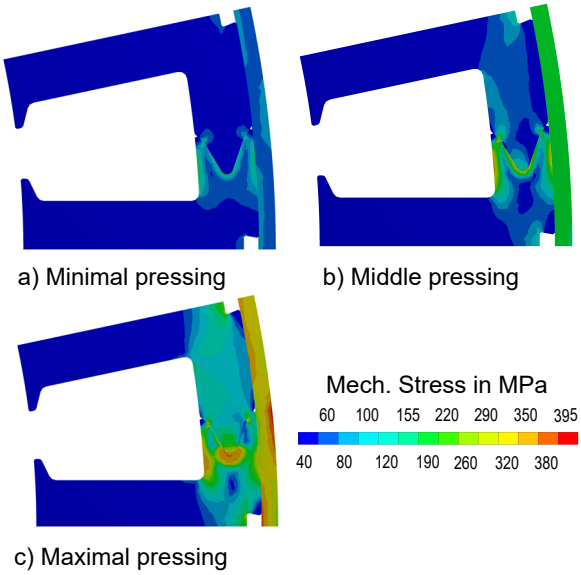

Fig. 6. Von Mises stress for the minimal, middle and maximal pressing.

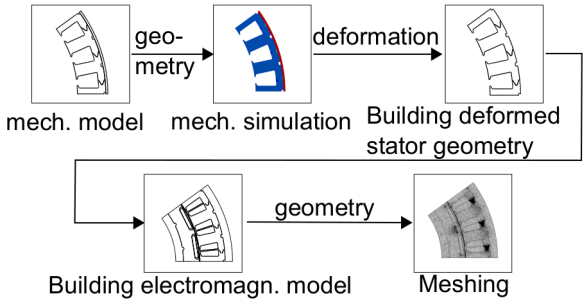

Fig. 7. Building procedure of electromagnetic model with consideration of deformation.

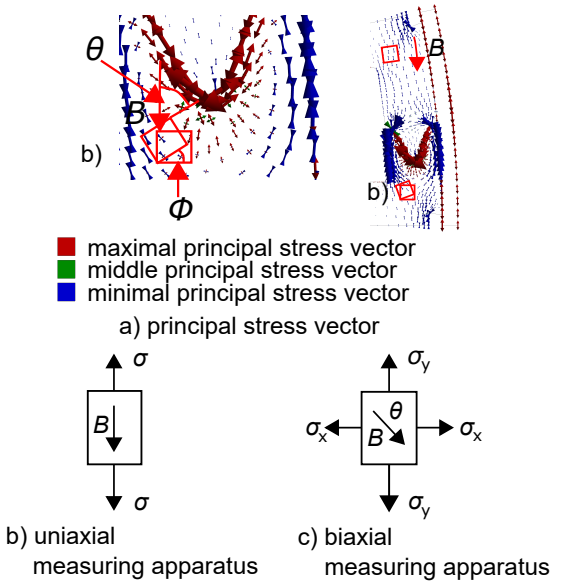

Fig. 8. Stress states of the mechanical simulation model.

simulation. The procedure is shown schematically in Figure 7.

A. Mechanical Stress State for Electromagnetic Simulation

Three stress components are required for the correct mapping of the stress behavior in a plane stress state (see Subsection III-C). In the yoke, a purely tangential tension occurs at some distance from the connecting notch (see Figure 8a)). The radial component and the shear stress component are negligibly small in this area. The magnetic flux density B in the stator yoke can be described, in a good approximation, by the tangential component. The material is thus magnetized in the direction parallel to the mechanical stress load. The mechanical stress state and the direction of magnetization of an element in this region of the stator can be well approximated by the measuring device from Subsection II-B.

In the area of the connecting notch, both radial and shear stress components are present. In the following, the stress and magnetization state of a single element is considered in Figure 8. As explained in Subsection III-A, the element can be transformed by coordinate transformation into a state without shear stress component. The two remaining stress components are principal stresses. The magnetic flux density in the considered element is no longer parallel to the mechanical stress load in the axial direction. Therefore, the rotation angle Θ of the transformation must be considered for a correct mapping of the magnetization behavior.

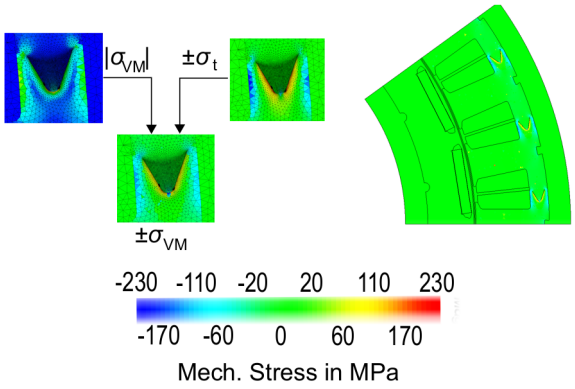

Fig. 9. Mapping of stress condition in electromagnetic simulation.

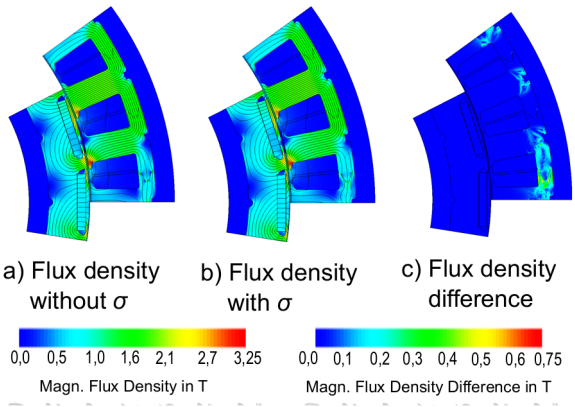

Fig. 10. Comparison of magnetic flux densities for simulation (a) with and (b) without consideration of mech. stress. (c) Flux density difference.

B. Methodology

The applied methodology is shown in Figure 9. The value for the mechanical stress is the von Mises stress value. For distinguishing between compressive and tensile loading, the sign of the tangential stress components is added to this value. This allows a mapping of the compressive and tensile stresses of the material without neglecting large portions of the stress state in the area of the connecting notch.

C. Magnetic Flux Density Distribution Inside the Connection Notch

For this study, the corner point ($I_{\mathrm{phase},1} = 320\,\mathrm{A}$, $\gamma = 210°$) is examined. This operating point describes the state of maximum torque, in which large areas of the stator iron are in saturation. Two simulations of the machine are performed to investigate the influence of mechanical stresses on the flux density distribution in the stator. In Figure 10, the magnetic flux density distribution of the two simulation models at the beginning of the electrical period is shown in the geometry. In addition, the difference in the flux densities of the two simulations is shown in Figure 10c.

The strongest difference in the flux density behavior can be seen in the region of the lower connecting notch of the pole pair. At the points where the spring and the tip are connected together and no air gap occurs, the flux density increases. In the area of the air gaps, the flux density is lower. The upper and middle connecting notch of the pole pair have a magnetic flux density of 1.8 T at which the material is in saturation. The air gap, which is in the range of 0.01 mm, is negligible in this case. At this point, there are no differences in the flux density between the two simulations at this operating point. The flux density is

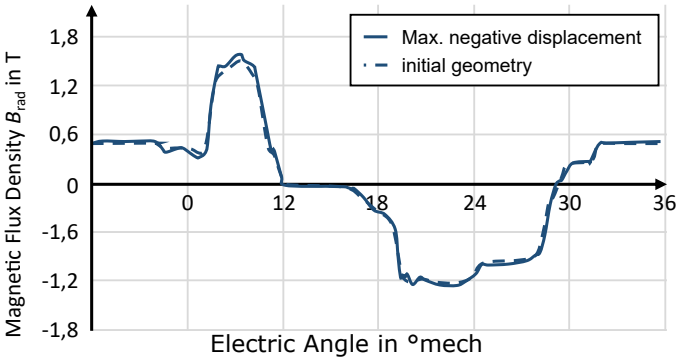

Fig. 11. Magnetic flux density inside air gap for initial geometry and maximale negative displacement.

equally distributed in the yoke for both cases.

When comparing the simulation taking into account the stress in Figure 10b with the simulation without consideration of the mechanical stresses in Figure 10a, the greatest changes occur in the area of production and connection notch on. In the area of the manufacturing notch, the mechanical stress of 50 MPa causes less flux in this area. Only in the area of the lower connecting notch. it is possible to detect a change in the magnetic flux density due to the mechanical stress. The material at the middle and upper connecting notches is at about 1.8 T in saturation. In saturation, the permeability is constant and independent of the mechanical stress. Accordingly, there are no changes in the flux density in this area. The lowest connecting notch has a magnetic flux density in the range of 0.8 T. In this range of magnetization, the mechanical stress has a significant influence on the flux density distribution in the notch. In the area of the connecting notch, flux density differences of up to 0.75 T occur (see Figure 10c). The flux is forced out of areas of high compressive and tensile load.

D. Magnetic Flux Density Distribution Inside the Air Gap

For the analysis of the flux density inside the air gap, the tolerance case of the maximum negative displacement at the air gap and the flux density of the undeformed initial geometry are compared. As described in Subsection III-C, the air gap height may vary up to 15 % due to tolerances of the compression bond. Figure 11 shows the flux density in the center of the air gap for the initial geometry and the deformed geometry at maximum negative displacement at the air gap.

In both cases, the stator model without connecting notch is used for the calculation and the mechanical stress behavior of the material is not taken into account. In the radial component of the magnetic flux density, an increase in the magnetic flux density due to the smaller air gap can be seen. Particularly in the area of tooth tips, the flux density increases by approximately 0.1 T. There is also an influence on the tangential flux density component, whereby only an increase occurs in the region of the tooth tips. The influence of the flux density changes due to the displacement and the mechanical stress are examined in the following sections regarding torque and iron losses.

E. Analysis of Torque

The mechanical stress of the material and the resulting change in the magnetization behavior of the material have hardly any influence on the torque of the machine. The torques with and without consideration of the mechanical stress in the case of nominal overfitting are almost identical for both operating points. Since no significant change in the magnetic flux density occurs for the other tolerance cases, it can be assumed that the mechanical stress has only a small influence on the torque of the machine, even for the tolerance cases of the minimum, nominal and maximum overfitting. Accordingly, the changed magnetization behavior of the material has no appreciable influence on the torque and causes only a changed flux path in the stator yoke in the vicinity of the connecting notches. Due to the displacement of the stator segments at the air gap is thus at a fluctuation of the air gap width to the ideal dimensions by 14.8 %, for the maximum torque of the machine by a fluctuation of the torque by 2.1 % can be assumed. For lower torques, the influence of the air gap width increases and the torque fluctuates up to 4 %. The results are consistent with other studies in this area [24].

F. Analysis of Iron Losses

This section examines the influence of stress on iron losses in the stator of the machine. The stress-dependency on the specific iron losses is described by the relation

$$p_{\mathrm{Fe}}(\sigma, B, f) = p_{\mathrm{stat}}(\sigma, B, f) + p_{\mathrm{dyn}}(\sigma, B, f)\,, \tag{1}$$

where p_{stat} describes the static and p_{dyn} the dynamic components of the iron losses [9]. They show dependencies on the mechanical stress σ, the magnetic flux density B and the frequency f. The static losses p_{stat} are calculated by

$$p_{\mathrm{stat}}(\sigma, B, f) = p_{\mathrm{hys}}(\sigma, B, f) = a_1(\sigma) \cdot B^{\alpha_0(\sigma)+\alpha_1(\sigma)\cdot B} \cdot f \tag{2}$$

and the dynamic losses by

$$p_{\mathrm{dyn}}(\sigma, B, f) = p_{\mathrm{cl}}(B, f) + p_{\mathrm{exc}}(\sigma, B, f) + p_{\mathrm{nl}}(\sigma, B, f)\,, \tag{3}$$

with

$$p_{\mathrm{cl}}(B, f) = a_2 \cdot B^2 \cdot f^2, \tag{4}$$

$$p_{\mathrm{exc}}(\sigma, B, f) = a_2 \cdot a_3(\sigma) \cdot B^{2+a_4(\sigma)} \cdot f^2 \text{ and} \tag{5}$$

$$p_{\mathrm{nl}}(\sigma, B, f) = a_5(\sigma) \cdot B^{1,5} \cdot f^{1,5}\,. \tag{6}$$

a_1 to a_5 are the stress-dependent loss parameters used to describe the individual loss components.

The stress-dependent loss parameters are determined according to [27]. Because of the stress-independent electrical conductivity of the eddy current parameter, it also remains stress-independent. The hysteresis curve is stretched for high compressive and tensile loads and compressed for small tensile loads. The hysteresis losses increase or decrease accordingly. The component of the excess losses also responds to a mechanical stress load.

With this method, the iron loss density in the stator yoke of the machine is investigated for the case of minimum, nominal, half and maximum overfitting. Subsequently, the iron losses of the four tolerance cases at the operating point are calculated and compared. The specific losses are shown in Figure 12 in the machine geometry for the selected operating point and the tolerance case of the nominal overpass.

Figure 12a shows the specific iron losses of the machine without consideration of the mechanical stress, Figure 12b with consideration of the mechanical tension and Figure 12c shows the difference between the two loss densities. The corresponding flux density solutions are used for the calculation with and without consideration of the mechanical stress.

In the stator yoke, an increase of the specific iron losses can be studied due to the compressive stress. In the area of the connecting notches occur both increase and decrease of the losses. First,

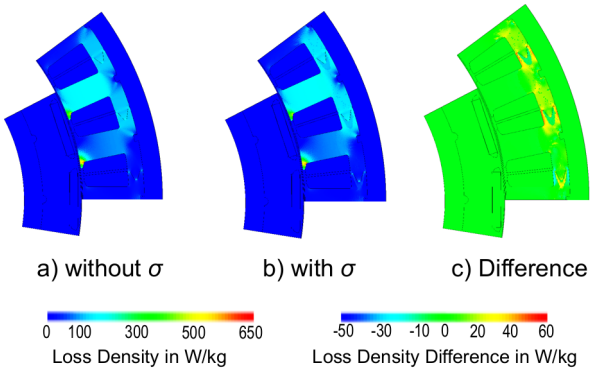

Fig. 12. Iron loss density (a) without and (b) with mechanical stress. (c) Iron loss density difference.

TABLE I. IRON LOSSES.

Tolerance Level	Iron losses w/o mech. stress	Iron losses w/ mech. stress	Difference
Minimum overfitting	816.00 W	858.60 W	5.26 %
Nominal overfitting	822.39 W	878.54 W	6.83 %
Half overfitting	810.98 W	900.20 W	11.00 %
Maximum overfitting	803.32 W	918.04 W	14.28 %

the lowest connecting notch of the pole pair is considered. At this connecting notch, a decrease in the loss density at the outer edges of the spring can be seen. In this area, an increase in losses is actually expected due to the compressive stress. The connecting notch has a flux density of approximately 0.8 T (see Figure 10). In this flux density region, due to the stress-dependent permeability, a shift of the flux density occurs in the region of the tensile stresses, which causes the flux density and thus also the iron losses at the outer edges of the spring to decrease compared to the simulation without consideration of the mechanical stress. Conversely, a decrease in iron losses is to be expected in the area of tensile stress. However, due to the shift in flux density, there is an increase in iron loss in this area.

In the middle and upper connecting notch, the stator yoke has a magnetic flux density of approximately 1.8 T (see Figure 10). In this flux density range, the flux density in the stator yoke is evenly distributed. At the outer edges of the spring, compressive stresses increase the iron loss density of 60 W kg^{-1}. In the area of tension, under the spring, the loss density decreases by -20 W kg^{-1} (see Figure 12).

Figure 13 shows the iron loss densities of the minimum, half, nominal, and maximum overpass tolerances at the central connecting notch. The area in which the iron losses decrease due to the favorable tensile stress, becomes smaller with increasing stress load. The areas in which the compressive stresses and the higher tensile stresses lead to an increase in iron loss, expand with increasing stress. In addition, it comes for the tolerance cases of half and the maximum overfitting, an increasing pressure load at the top of the connecting notch. In the case of maximum overfitting, this leads to an increase of 80 W kg^{-1} at the top (compare Figure 13d).

The iron losses of the machine averaged over an electrical period are summarized in Table I for the four cases investigated.

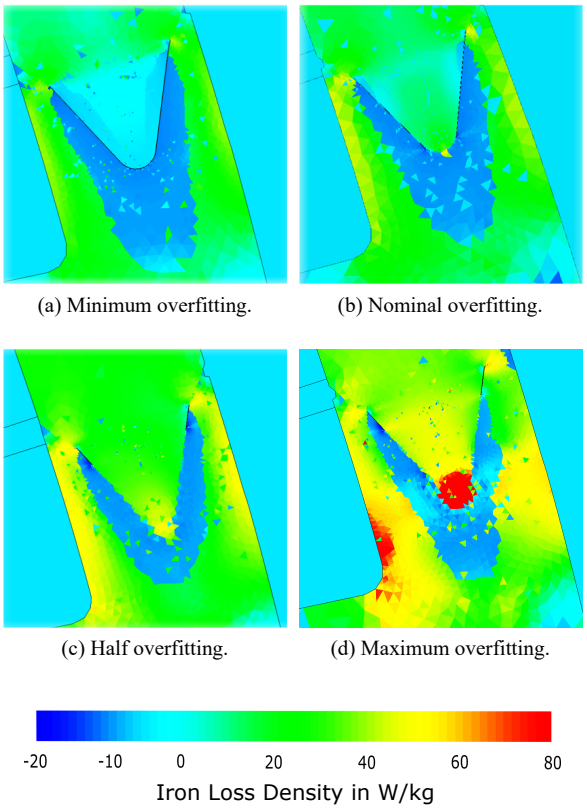

Fig. 13. Iron loss densities at the central connection notch of the(a) minimum, (b) nominal, (c) half and (d) maximum overfitting tolerances.

Even without consideration of mechanical stress, the four cases show different iron losses. In the case of nominal overfitting these are about 20 W larger than the maximum overfitting. This difference is due to the different air gap widths of the four tolerance cases, which have an influence on the magnetic flux density B in the stator. This influence is much more pronounced in the iron losses than in the torque, since the flux density is exponential in the iron loss calculation. The iron losses increase significantly, taking into account the mechanical stress. The iron losses taking into account the mechanical stresses decrease in percentage of the iron losses, without considering the mechanical stress, from the percentage of 5.26 % at the minimum overpass to 14.28 % for the maximum overfit.

V. CONCLUSIONS

The construction of a segmented stator in a fit assembly leads to a deformation and a mechanical stress on the electrical steel. The mechanical simulation shows a mechanical stress load, which fluctuates by more than 100 MPa due to tolerance influences. The resulting displacement at the tip of the tooth in this case leads to a possible air gap fluctuation of over 15 % relative to the ideal geometry. Transmitted to the electromagnetic simulation, this shows the main influence on the maximum torque at the corner point of the electrical machine. The mechanical stresses have a negligible influence on the torque. However, the iron losses of the machine are influenced by the air gap height and by the mechanical stresses as well. Taking into account the mechanical stresses, the losses increase up to 15 %, compared to simulations without considering the mechanical stresses.

For future investigations, the method for determining the material behavior under tensile and compressive loading must be improved so that a further range of stresses can be measured. Of particular interest here are measuring devices that can make a field distribution perpendicular to the mechanical load.

References

[1] A. Füßel, “Technische Potenzialanalyse der Elektromobilität”, Springer Vieweg, 2017.

[2] A. Eilenberger, M. Schrödl, F. Demmelmayr, “Elektrofahrzeuge mit Permanentmagnet-Synchronmaschinen”, e&i Elektrotechnik und Informationstechnik, no. 1, vol. 128, pp. 40–46, 2011.

[3] J. Shen, C. Wang, D. Miao, M. Jin, D. Shi, Y. Wang, “Analysis and Optimization of a Modular Stator Core with Segmental Teeth and Solid Back Iron for PM Electrical Machines”, Electrical Machines & Drives Conference (IEMDC), pp. 1270–1275, 2011.

[4] M. Neubauer, H. Neudorfer, “Besonderheiten hochausgenutzter Traktionsmaschinen mit kurzer Baulänge”, e&i Elektrotechnik und Informationstechnik, no. 1, vol. 132, pp. 18–24, 2015.

[5] J. Wang, X. Yuan, K. Atallah, “Design Optimization of a Surface-Mounted Permanent-Magnet Motor With Concentrated Windings for Electric Vehicle Applications”, IEEE Transactions on Vehicular Technology, no. 3, vol. 62, pp. 1053–1064, 2013.

[6] T. Albrecht, C. Gürsel, E. Lamprecht, T. Klier, “Joining Techniques of the Rotor Segmentation of PM-Synchronous Machines for Hybrid Drives”, Proceedings: 2nd International Electric Drives Production Conference, 2012.

[7] J. Franke, T. Albrecht, E. Lamprecht, M. Hubert, M. Schneider, “The Development and Validation of a Segmented Rotor Design for Electric Motors in Hybrid Vehicle Applications”, Internation Symposium on Power Electronics, Electrical Drives, Automation and Motion, SPEEDAM, pp. 106–111, 2014.

[8] N. Leuning, S. Steentjes, M. Schulte, W. Bleck, K. Hameyer, “Effect of elastic and plastic tensile mechanical loading on the magnetic properties of NGO electrical steel”, Journal of Magnetism and Magnetic Materials, vol. 417, pp. 42–48, 2016.

[9] J. Karthaus, S. Steentjes, K. Hameyer, “Mechanical stress-dependency of iron losses in non-oriented electrical steel sheets”, Proceedings: XXIV Symposium Electromagnetic Phenomena in Nonlinear Circuits, pp. 111–112, 2016.

[10] H. Naumoski, A. Maucher, U. Herr, “Investigation of the influence of global stresses and strains on the magnetic properties of electrical steels with varying alloying content and grain size”, Proceedings: 5th International Electric Drives Production Conference, pp. 1–8, 2015.

[11] B. Cullity, C. Graham, “Introduction to magnetic materials”, 2. Auflage, Wiley-IEEE Press, 2003.

[12] DIN IEC 60404-3, “Magnetische Werkstoffe - Teil3: Verfahren zur Bestimmung der magnetischen Eigenschaften von Elektroband und -blech mit Hilfe eines Tafelmessgerätes”, 2010.

[13] N. Leuning, S. Steentjes, K. Hameyer, “Effect of magnetic anisotropy on villary effect in non-oriented FeSi electrical steel”, International Journal of Applied Electromagnetics and Mechanics, no. 1, vol. 55, pp. 23–31, 2017.

[14] D. Miyagi, N. Maeda, Y. Ozeki, K. Miki, N. Takahashi, “Estimation of Iron Loss in Motor Core with Schrink Fitting Using FEM Analysis”, IEEE Transactions on Magnetics, no. 3, vol. 45, pp. 1704–1707, 2009.

[15] J. Makar, B. Tanner, “The effect of plastic deformation and residual stress on the permeability and magnetostriction of steels”, Journal of Magnetism and Magnetic Materials, no. 3, vol. 222, pp. 291–304, 2000.

[16] G. von Pfingsten, D. Paul, K. Hameyer, “Influence of Axial Mechanical Stress on the Magnetic Properties of Non-Oriented Electrical Steel”, 6th International Electric Drive Production Conference (EDPC), pp. 193–200, Nürnberg, 2016.

[17] C. Gebhardt, “Praxisbuch FEM mit Ansys Workbech: Einführung in die lineare und nichtlineare Mechanik”, 2. Überarbeitete Auflage, Hanser, 2014.

[18] P. Wriggers, “Technische Mechanik kompakt: Starrkörperstatik Elastostatik Kinetik”, 2. durchgeschaute und überarbeitete Auflage, B. G. Teubner Verlag | GWV Fachverlage GmbH, 2006.

[19] ANSYS (Hrsg.), “Ansys Mechanical Structural Nonlinearities: Introduction to Contact”, 2010.

[20] E. L. Gaertner, M. G.d. Bortoli, “Some Aspects for the Simulation of a Non-Linear Problem with Plasticity and Contact”, Proceedings: 134. International Ansys Conference, 2006.

[21] G. Gottstein, “Materialwissenschaft und Werkstofftechnik: Physikalische Grundlagen”, 4. neu bearbeitete Auflage, Springer Vieweg, 2014.

[22] S. Thomas, “Konstitutive Gleichungen und numerische Verfahren zur Beschreibung von Verformung und Schädigung”, Dissertation, Technische Universität Darmstadt, 2001.

[23] M. Linke, E. Nast, “Festigkeitslehre für den Leichtbau”, Springer Vieweg, 2015.

[24] M. Balluff, H. Naumoski, K. Hameyer, “Sensitivity analysis on tolerance induced torque fluctuation of a synchronous machine”, Proceedings: 6th International Electric Drives Production Conference, pp. 128–134, 2016.

[25] L. Petkovska, G. Cvetkovski, “Performance Optimization of a Permanent Magnet Synchronous Motor by Sampling Based Sensitivity Analysis”, Proceedings: International Conference on Electrical Machines, 2008.

[26] Z. Wu, H. Guo, H. Qian, D. Wang, “Sensitive Analysis of Geometrical Parameters on Robust Design for Surface Mounted Permanent Magnet Synchronous Motor”, Proceedings: International Conference on Electrical Machines and Systems, pp. 1169–1173, 2013.

[27] J. Karthaus, S. Steentjes, N. Leuning, K. Hameyer, “Effect of mechanical stress on different iron loss components up to high frequencies and magnetic flux densities”, COMPEL – The international journal for computation and mathematics in electrical and electronic engineering, no. 3, vol. 36, pp. 580–592, 2017.

VI. Authors Name and Affiliation

Jan Karthaus, Institute of Electrical Machines, RWTH Aachen University, Schinkelstrasse 4, D-52062 Aachen, Germany, +49 241 80 93962,
jan.karthaus@iem.rwth-aachen.de.

Markus Balluff, Integrated E-Drives, Daimler AG, D-71059 Sindelfingen, Germany, +49 176 309 30520,
markus.balluff@daimler.com.

Michael Schröder, Institute of Electrical Machines, RWTH Aachen University, Schinkelstrasse 4, D-52062 Aachen, Germany, +49 241 80 97638,
michael.schroeder@iem.rwth-aachen.de.

Martin Gerlach, Institute for Drive Systems and Power Electronics, Leibniz Universität Hannover, Welfengarten 1, D-30167 Hannover, Germany, +49 511 762 2863,
martin.gerlach@ial.uni-hannover.de.

Kay Hameyer, Institute of Electrical Machines, RWTH Aachen University, Schinkelstrasse 4, D-52062 Aachen, Germany, +49 241 80 97667,
kay.hameyer@iem.rwth-aachen.de.